

# An Efficient Sweep-based Solver for the $S_N$ Equations on High-Order Meshes

T. S. Haut,<sup>\*,a</sup> P. G. Maginot,<sup>b</sup> V. Z. Tomov,<sup>a</sup>  
B. S. Southworth,<sup>c</sup> T. A. Brunner,<sup>b</sup> and T. S. Bailey<sup>b</sup>

<sup>a</sup> *Center for Applied Scientific Computing, Lawrence Livermore National Lab*  
*P. O. Box 7000, Livermore, CA 94551*

<sup>b</sup> *Design Physics Division, Lawrence Livermore National Lab*  
*P. O. Box 7000, Livermore, CA 94551*

<sup>c</sup> *Department of Applied Mathematics, University of Colorado*  
*Engineering Center, ECOT 225, 526 UCB, Boulder, CO 80309-0526*

\*Email: <mailto:haut3@llnl.gov>

Number of pages: 26

Number of tables: 6

Number of figures: 8

### **Abstract**

We propose a graph-based sweep algorithm for solving the steady state, mono-energetic discrete ordinates on meshes of high-order curved mesh elements. Our spatial discretization consists of arbitrarily high-order discontinuous Galerkin finite elements using upwinding at mesh element faces. To determine mesh element sweep ordering, we define a directed, weighted graph whose vertices correspond to mesh elements, and whose edges correspond to mesh element upwind dependencies. This graph is made acyclic by removing select edges in a way that approximately minimizes the sum of removed edge weights. Once the set of removed edges is determined, transport sweeps are performed by lagging the upwind dependency associated with the removed edges. The proposed algorithm is tested on several 2D and 3D meshes composed of high-order curved mesh elements.

**Keywords** — transport, discrete ordinates, high-order, sweep, unstructured

## I. INTRODUCTION

Hydrodynamics discretizations that leverage high-order (HO) curved meshes have become increasingly popular in recent years, due to several mathematical and computational advantages they afford. For example, HO meshes can more accurately model curved geometries, and consequently simulations that use HO meshes can use significantly fewer mesh elements to achieve an equivalent accuracy in comparison to low-order (i.e. straight-edged) meshes. HO meshes are essential for achieving optimal finite element convergence rates (for smooth problems) on domains with curved boundaries or interfaces, in both the Lagrangian [8, 7, 11] and arbitrary Lagrangian-Eulerian (ALE) [5, 3] contexts. Additionally, HO meshes permit better spherical symmetry preservation for implosion calculations in axisymmetric geometries [7].

In the context of radiation transport, HO methods have the potential for reducing the prohibitively large number of spatial unknowns required to resolve the radiation’s seven-dimensional phase space (three in space, two in angle, energy, and time). The need to reduce the number of thermal radiation transport (TRT) unknowns is further magnified with the rise of memory motion/communication-bound next-generation architectures such as the graphics processing unit based machine Sierra [6]. The ability to solve the TRT equations on HO curved meshes is further motivated when one is interested in the simulation of multi-physics phenomena, such as inertial confinement fusion, using HO hydrodynamics methods, such as those in [8, 7, 11, 5, 3]. Such radiation-hydrodynamics simulations must preserve the equilibrium diffusion limit, which requires the solution of the  $S_N$  equations on a mesh compatible with the HO hydrodynamics mesh.

One possibility to achieve the required radiation hydrodynamics coupling would be to interpolate fields such as the radiation energy density between a HO representation on the hydrodynamics mesh and a field discretized with linear elements on a refined, low-order (LO) TRT specific mesh. However, this would necessitate a significant increase in TRT degrees-of-freedom to “straighten out” the HO hydrodynamics meshes. Additionally, (i) no analysis currently exists proving that such a scheme preserves the equilibrium diffusion limit, and (ii) interpolating between LO and HO representations of the same field will likely lead to decreased robustness, stability, and physics fidelity.

An alternative approach is to solve the TRT equations directly on the HO mesh using a spatial discretization for the TRT equations that is consistent with the thermodynamic variables

of the hydrodynamics discretization. In [8, 7, 3], the hydrodynamics’ thermodynamic variables are discretized in space by a discontinuous Galerkin (DG) formulation. Solving the TRT equations directly on the hydrodynamics mesh is most consistent with historical precedent for robust radiation hydrodynamics coupling stability [10]. Further, when the TRT unknowns and the hydrodynamics’ thermodynamic unknowns have identical centerings, it is likely that even better multi-physics robustness, numerical stability, and accuracy can be achieved. In particular, Woods and Palmer have shown that an upwinded DG spatial discretization of the mono-energetic, steady-state,  $S_N$  angular discretization of the linear Boltzmann equation (i) yields HO convergence [28, 27] and (ii) maintains the thick diffusion limit [29, 27]. Spatial discretizations of the TRT equations that preserve the thick diffusion limit are tantamount to spatial discretizations that will preserve the equilibrium diffusion limit when applied to time-dependent, multi-frequency,  $S_N$  angular approximations to the non-linear thermal radiative transfer equations [19, 2]. Hereafter, we refer to the spatially analytic mono-energetic, steady-state,  $S_N$  angular discretizations of the linear Boltzmann equation simply as the linear transport equations.

When source iteration [14] is used to iteratively solve for particle scattering, each iteration requires solving the linear transport equation (independently) for each angle. Upwinded spatial discretizations of the linear transport equations on product meshes of orthogonal mesh elements (or on general 2d, convex meshes), lead to a block lower-triangular set of equations, in some ordering, for each angle. This system can be solved on an element-by-element basis by doing a block forward solve of the corresponding matrix; in the the transport literature, this is referred to as a “transport sweep.” On meshes of non-orthogonal linear (straight-edged) mesh elements, upwinded DG discretizations of the linear transport equations do not necessarily form lower-triangular systems of equations. Systems with upper-triangular components are often produced by discretizations on 3D linear unstructured grids [26], or by discretizations on 2D linear meshes that contain concave elements. Nevertheless, it is usually possible to choose a mesh ordering that results in a nearly block lower-triangular matrix whose inverse is approximated well in a transport sweep [18, 20, 22, 21]. Such an algorithm is equivalent to an ordered block Gauss-Seidel iteration on the upwinded DG equations.

On HO curved meshes, an upwind discretization of the linear transport equations can result in significantly more upper triangular entries, compared to similar problems composed on linear

mesh elements. As an example, it is possible to have two neighboring HO mesh elements that are both upwind of each other, even in 2D. Thus, in HO meshes, strongly connected components (SCCs) of mesh elements are expected to be more prevalent and larger than SCCs appearing in linear meshes. Each SCC corresponds to a non-triangular component of the spatially discretized linear transport equations. As mesh element order increases, such SCCs likely grow in size and number, causing convergence of a naive Gauss-Seidel iteration to suffer. To that end, methods for determining a mesh element ordering that minimizes the size of these SCCs takes on greater importance with HO curved meshes.

The main purpose of this paper is to develop and present a transport sweep algorithm based on a quasi-optimal mesh-element ordering for a block Gauss-Seidel iteration. In particular, we extend the graph-based methods of [18, 20, 22, 21] to HO curved meshes in a manner that directly connects the graph to both the mesh topology and HO DG spatial discretization. After defining such a graph, a transport-sweep mesh-element ordering is determined so that the “optimal” approximation of the inverse of the upwinded DG discretization can be applied on an element-by-element basis. In graph-theoretic terms, we construct the maximum acyclic subgraph by removing edges in the dependency graph until the modified graph is acyclic using a heuristic that (approximately) minimizes the weight of removed edges. Performance of this graph based, approximate transport sweep algorithm is then demonstrated on a variety of test problems, including an annulus embedded in a square domain, reminiscent of the canonical light-water reactor pin cell [4]; a HO 2D-mesh derived from a HO Lagrangian simulation of the “triple point” problem [8, 12]; and a 3D extension of the 2D, single-mode, Rayleigh-Taylor instability problem presented in [8]. In this series of test problems, the iteration count of our Gauss-Seidel, quasi-optimal element-by-element transport sweep solver is compared against the number of iterations required for solution of the exact upwinded DG equations via an approximate ideal restriction algebraic multigrid solver (AIR) [16, 17, 13]. Finally, we compare the unknown count, iteration count, and accuracy of our Gauss-Seidel iteration on the HO mesh to refined meshes of linear mesh elements using a linear upwinded DG transport discretization.

## II. SPATIAL DISCRETIZATION OF THE LINEAR TRANSPORT EQUATIONS

In this work, we focus on the solution of the steady-state, mono-energetic discrete ordinates linear Boltzmann equations,

$$\begin{aligned} \boldsymbol{\Omega}_d \cdot \nabla_{\mathbf{x}} \psi_d(\mathbf{x}) + \sigma_t(\mathbf{x}) \psi_d(\mathbf{x}) &= \frac{\sigma_s(\mathbf{x})}{4\pi} \varphi(\mathbf{x}) + q_d(\mathbf{x}), \quad \mathbf{x} \in \mathcal{D} \\ \psi_d(\mathbf{x}) &= \psi_{d,\text{inc}}(\mathbf{x}), \quad \mathbf{x} \in \partial\mathcal{D} \quad \text{and} \quad \mathbf{n}(\mathbf{x}) \cdot \boldsymbol{\Omega}_d < 0. \end{aligned} \quad (1)$$

In (1),  $\mathcal{D}$  is a domain in  $dim$  dimensions and  $\partial\mathcal{D}$  is its boundary;  $\psi_d(\mathbf{x})$  is the angular flux  $\left[ \frac{n}{cm^2 - sec - ster} \right]$  in the direction of discrete ordinate  $\boldsymbol{\Omega}_d$ , with  $\boldsymbol{\Omega}_d \in \mathbb{S}^2$ ; the total macroscopic interaction cross section,  $\sigma_t(\mathbf{x}) [cm^{-1}]$ , is the sum of the macroscopic absorption cross section,  $\sigma_a(\mathbf{x}) [cm^{-1}]$ , and the scattering macroscopic cross section,  $\sigma_s(\mathbf{x}) [cm^{-1}]$ ; scattering is assumed to be isotropic; we have assumed the validity of the discrete ordinates approximation to the scalar flux,  $\varphi \left[ \frac{n}{cm^2 - sec} \right]$ ,

$$\varphi(\mathbf{x}) \approx \sum_{d=1}^{N_\Omega} \omega_d \psi_d(\mathbf{x}) ; \quad (2)$$

$q_d(\mathbf{x}) \left[ \frac{n}{cm^3 - sec - ster} \right]$  is a volumetric source in the direction of  $\boldsymbol{\Omega}_d$ ;  $\psi_{d,\text{inc}}(\mathbf{x})$  is a known, incident angular flux on the boundary  $\partial\mathcal{D}$  of domain  $\mathcal{D}$ ; and  $\mathbf{n}(\mathbf{x})$  is the outward directed unit normal on  $\partial\mathcal{D}$  at  $\mathbf{x}$ . Additionally, we have chosen the set of angular quadrature weights and directions,  $\{(\omega_d, \boldsymbol{\Omega}_d)\}_1^{N_\Omega}$ , such that all  $\omega_d > 0$  and  $\sum_{d=1}^{N_\Omega} \omega_d = 4\pi$ .

**Discrete representation of the HO mesh.** Equation (1) is discretized over a HO curved mesh. Let  $\cup \kappa_e$  denote a tessellation of physical space using HO mesh elements,  $\{\kappa_e\}_1^{N_\kappa}$ , each being of order  $r$ . Consider a set of scalar Lagrangian finite element basis functions  $\{\hat{v}_m(\xi)\}_1^{N_v}$  defined on the reference element  $\hat{\kappa}$ . For simplicial elements (triangles and tetrahedrons), the basis  $\{\hat{v}_m\}$  spans  $P_r$ , the space of all polynomials of total degree at most  $r$ ; for tensor product elements (quadrilaterals and hexahedrons)  $\{\hat{v}_m\}$  is chosen to be a basis for  $Q_r$ , the space of all polynomials of degree at most  $r$  in each variable. The shape of any element  $\kappa_e$  in the mesh is then fully described by a matrix  $\mathbf{x}_e$  of size  $dim \times N_v$  whose columns represent the coordinates of the element control points (aka element degrees of freedom). Given  $\mathbf{x}_e$ , the position of  $\kappa_e$  (corresponding to a point  $\xi$  in  $\hat{\kappa}$ ) is derived via the mapping  $\mathbf{T}_e : \hat{\kappa} \rightarrow \kappa_e$ :

$$\mathbf{x}_e(\boldsymbol{\xi}) = \mathbf{T}_e(\boldsymbol{\xi}) = \sum_{m=1}^{N_v} \mathbf{x}_{e,m} \hat{v}_m(\boldsymbol{\xi}), \quad \mathbf{x}_{e,m} = \mathbf{T}_e(\boldsymbol{\xi}_m), \quad (3)$$

where we use  $\mathbf{x}_{e,m}$  to denote the  $m$ -th column of  $\mathbf{x}_e$ . When two elements  $\kappa_e$  and  $\kappa_{e'}$  share a common mesh entity (vertex, edge, or face) then their control-point matrices  $\mathbf{x}_e$  and  $\mathbf{x}_{e'}$  are not independent because, to ensure mesh continuity, the descriptions of the common entity (through  $\mathbf{T}_e$  on one hand and  $\mathbf{T}_{e'}$  on the other) must coincide. This type of interdependence among mesh elements is typically expressed by defining a global vector  $\mathbf{x}$  of control points (degrees of freedom) and a set of linear operators  $\mathbf{x} \rightarrow \mathbf{x}_e$ , one per mesh element, that define/extract the local coordinates  $\mathbf{x}_e$  from the global vector  $\mathbf{x}$ . Thus, the global continuity of the mesh is ensured for any value of  $\mathbf{x}$ .

**Discontinuous Galerkin formulation.** We spatially discretize (1) using HO DG approximations of  $\psi_d(\mathbf{x})$  and  $\varphi(\mathbf{x})$ . Let  $\{\hat{u}_m(\boldsymbol{\xi})\}_1^{N_u}$  be a set of scalar Lagrangian finite element basis functions defined on the reference element  $\hat{\kappa}$ . As before, this basis spans  $P_s$  or  $Q_s$  for simplicial and tensor elements, respectively, where  $s$  is the DG finite element order. For a given element  $\kappa_e$  in physical space, the corresponding basis functions,  $\{u_m^e(\mathbf{x})\}_1^{N_u}$ , are defined through

$$u_m^e(\mathbf{x}_e(\boldsymbol{\xi})) \equiv \hat{u}_m(\boldsymbol{\xi}), \quad \boldsymbol{\xi} \in \hat{\kappa}. \quad (4)$$

Regardless of the particular mesh element, each  $u_m^e$  satisfies  $u_m^e(\mathbf{x}_n) = \delta_{m,n}$ , where  $\mathbf{x}_n$  is the nodal position of the  $n$ -th basis function. These basis functions are used to discretize the angular flux and scalar flux on any element  $\kappa_e$  as

$$\tilde{\psi}_e^d(\mathbf{x}) = \sum_{m=1}^{N_u} \psi_{e,m}^d u_m^e(\mathbf{x}),$$

and

$$\tilde{\varphi}_e(\mathbf{x}) = \sum_{m=1}^{N_u} \varphi_{e,m} u_m^e(\mathbf{x}).$$

On a face  $\Gamma_{e,e'}$  between neighboring mesh elements  $e$  and  $e'$ , upwinding is used to define the angular flux,

$$\tilde{\psi}_{e,e'}^d(\mathbf{x}) = \begin{cases} \tilde{\psi}_e^d(\mathbf{x}) & \text{if } \boldsymbol{\Omega}_d \cdot \mathbf{n}_e(\mathbf{x}) \geq 0, \\ \tilde{\psi}_{e'}^d(\mathbf{x}) & \text{if } \boldsymbol{\Omega}_d \cdot \mathbf{n}_e(\mathbf{x}) < 0, \end{cases}$$

where  $\mathbf{n}_e(\mathbf{x})$  is the outward directed normal of  $\kappa_e$  that point into  $\kappa_{e'}$ . Following the standard Galerkin procedure the DG discretization described above yields the following matrix equation,

$$G^{(d)}\boldsymbol{\psi}^{(d)} + F^{(d)}\boldsymbol{\psi}^{(d)} + M_t\boldsymbol{\psi}^{(d)} - \frac{1}{4\pi}M_s\boldsymbol{\varphi} = \mathbf{q}^{(d)}, \quad (5)$$

where  $\boldsymbol{\psi}^{(d)}$  and  $\boldsymbol{\varphi}$  are the vectors storing the degree of freedom (DOF) values  $\{\psi_{e,m}^d\}$  and  $\{\varphi_{e,m}\}$ ,  $e = 1 \dots N_\kappa, m = 1 \dots N_u$ . The matrices  $G^{(d)}$ ,  $F^{(d)}$ ,  $M_t$ , and  $M_s$  are block-diagonal by mesh element indexing;  $\mathbf{q}^{(d)}$  is also a block-diagonal vector. Indexing DOFs using  $m$  and  $n$  within a mesh element  $\kappa_e$ , the individual blocks of  $G^{(d)}$ ,  $M_t$ , and  $M_s$  are, respectively,

$$\left[G_e^{(d)}\right]_{m,n} = - \int_{\kappa_e} (\boldsymbol{\Omega}_d \cdot \nabla_{\mathbf{x}} u_m^e) u_n^e d\mathbf{x}, \quad (6)$$

$$[M_{t,e}]_{m,n} = \int_{\kappa_e} \sigma_t(\mathbf{x}) u_m^e u_n^e d\mathbf{x} \quad (7)$$

$$[M_{s,e}]_{m,n} = \int_{\kappa_e} \sigma_s(\mathbf{x}) u_m^e u_n^e d\mathbf{x}. \quad (8)$$

The source spatial moments vector,  $\mathbf{q}^{(d)} = \{q_{e,m}^{(d)}\}$ , is given by

$$q_{e,m}^{(d)} = \int_{\kappa_e} q_d(\mathbf{x}) u_m^e d\mathbf{x} - \int_{\partial\kappa_e \cap \partial\mathcal{D}} \frac{1}{2} (\boldsymbol{\Omega}_d \cdot \mathbf{n}_e + |\boldsymbol{\Omega}_d \cdot \mathbf{n}_e|) u_m^e \psi_{d,\text{inc}}^{(d)} ds. \quad (9)$$

The face matrix in (5),  $F^{(d)}$ , has both block-diagonal components,  $F_e^{(d)}$ ,

$$\left[F_e^{(d)}\right]_{m,n} = \int_{\Gamma_{e,e}} \left( \frac{1}{2} \boldsymbol{\Omega}_d \cdot \mathbf{n}_e + \frac{1}{2} |\boldsymbol{\Omega}_d \cdot \mathbf{n}_e| \right) u_m^e u_n^e ds, \quad (10)$$

as well as off-diagonal block components,  $F_{e,e'}^{(d)}$ . For two neighboring mesh elements  $\kappa_e$  and  $\kappa_{e'}$  that share face  $\Gamma_{e,e'}$ ,  $F_{e,e'}^{(d)}$  is defined as

$$\left[F_{e,e'}^{(d)}\right]_{m,n} = \int_{\Gamma_{e,e'}} \left( \frac{1}{2} |\boldsymbol{\Omega}_d \cdot \mathbf{n}_e| - \frac{1}{2} \boldsymbol{\Omega}_d \cdot \mathbf{n}_e \right) u_m^e u_n^{e'} ds, \quad e' \neq e. \quad (11)$$

It is critical to remember that in (10) and (11),  $\mathbf{n}_e$  points from element  $\kappa_e$  into  $\kappa_{e'}$ , *always*.

The individual blocks defined in (6)-(8) can be expressed in terms of integration over the reference element  $\hat{\kappa}$  using the mesh element transformation defined in (3),

$$\left[G_e^{(d)}\right]_{m,n} = - \int_{\hat{\kappa}} (\boldsymbol{\Omega}_d \cdot J^{-T}(\boldsymbol{\xi}) \nabla_{\boldsymbol{\xi}} \hat{u}_m) \hat{u}_n |J^e(\boldsymbol{\xi})| d\boldsymbol{\xi} , \quad (12)$$

$$[M_{t,e}]_{m,n} = \int_{\hat{\kappa}} \sigma_t \hat{u}_m \hat{u}_n |J^e(\boldsymbol{\xi})| d\boldsymbol{\xi} , \text{ and} \quad (13)$$

$$[M_{s,e}]_{m,n} = \int_{\hat{\kappa}} \sigma_s \hat{u}_m \hat{u}_n |J^e(\boldsymbol{\xi})| d\boldsymbol{\xi} , \quad (14)$$

where  $J$  is the Jacobian matrix of the coordinate matrix defined in (3):

$$J^e(\boldsymbol{\xi}) = \frac{\partial \mathbf{T}_e(\boldsymbol{\xi})}{\partial \boldsymbol{\xi}} = \sum_{m=1}^{N_v} \mathbf{x}_{e,m} [\nabla \hat{u}_m(\boldsymbol{\xi})]^T . \quad (15)$$

Likewise, the  $F^{(d)}$  block element can be evaluated on a reference element,

$$\left[F_e^{(d)}\right]_{m,n} = \int_{\hat{\Gamma}} \left( \frac{1}{2} \boldsymbol{\Omega}_d \cdot \mathbf{n}_e + \frac{1}{2} |\boldsymbol{\Omega}_d \cdot \mathbf{n}_e| \right) \hat{u}_m \hat{u}_{n'} |J^\Gamma(\hat{\mathbf{s}})| d\hat{\mathbf{s}}, \quad (16)$$

$$\left[F_{e,e'}^{(d)}\right]_{m,n} = \int_{\hat{\Gamma}} \left( \frac{1}{2} |\boldsymbol{\Omega}_d \cdot \mathbf{n}_e| - \frac{1}{2} \boldsymbol{\Omega}_d \cdot \mathbf{n}_e \right) \hat{u}_m \hat{u}_{n'} |J^\Gamma(\hat{\mathbf{s}})| d\hat{\mathbf{s}} . \quad (17)$$

In (17) and 16,  $n'$  is used in the reference element integration to emphasize that the reference element indexing in mesh element  $\kappa_e$  is not the same as in  $\kappa_{e'}$ . The face Jacobian  $J^\Gamma$  is derived through the  $dim - 1$  versions of (3) and (15).

The integrands in (12)-(17) are typically evaluated using numerical quadrature. In particular, Gauss-Legendre quadrature is often used with great success to evaluate the polynomial (assuming constant material properties) integrands of (12)-(14). However, for linear mesh elements in 3D, and more generally HO mesh elements in multi-dimensional geometry, (16) and (17) have non-smooth integrands. The  $F_e^{(d)}$  and  $F_{e,e'}^{(d)}$  integrands are non-smooth on re-entrant faces where  $\boldsymbol{\Omega}_d \cdot \mathbf{n}_e$  changes sign. In such cases standard quadrature schemes designed to integrate smoothly varying functions can converge slowly. To achieve a simple and rapidly convergent integration scheme, one can use

Romberg integration to rapidly evaluate the piecewise smooth integrands of (16)-(17) [23].

### III. GRAPH-BASED TRANSPORT SWEEP ALGORITHM

We now describe the manner in which we solve (5). First, we note that while it is possible to solve the linear system described by (5), the coupling of all  $\psi^{(d)}$  to all other directions implied by the definition of (2) requires that the angular flux for every direction be solved simultaneously, a computationally intractable feat for all but the coarsest of problem resolutions. Rather than solve for the  $N_\Omega$  angular fluxes simultaneously, (5) is typically solved using fixed point iteration,

$$\left[ G^{(d)} + F^{(d)} + M_t \right] \boldsymbol{\psi}_{(\ell+1)}^{(d)} = \mathbf{q}^{(d)} + \frac{1}{4\pi} M_s \boldsymbol{\varphi}_{(\ell)} \quad (18)$$

where for iteration index  $\ell$ , (18) is used to lag the angle coupling,

$$\boldsymbol{\varphi}_{(\ell)} = \sum_{d=1}^{N_\Omega} \omega_d \boldsymbol{\psi}_{(\ell)}^{(d)}.$$

Equation (18) is typically referred to as source iteration in transport literature [14]. While it is more tractable to solve (18) by forming and exactly applying the “streaming + collision operator”

$$\left[ G^{(d)} + F^{(d)} + M_t \right], \quad (19)$$

or left hand side of (18), it is more common to invert the streaming+collision operator for each angle on a mesh element-by-mesh element basis in what is referred to as a transport sweep. In the following discussion we assume that, for a given direction  $\boldsymbol{\Omega}_d$ , each mesh element index corresponds to the order in which the unknowns are solved. In 2D, for convex domains discretized with convex mesh elements, or for Cartesian product meshes in both 2D and 3D, it is always possible to choose a mesh element ordering for which the face matrix  $F_{e,e'}^{(d)} = 0$  whenever  $e' > e$ . In this case, the “streaming + collision operator” is block lower-triangular. Its exact inverse can be applied by solving (5) element-by-element, in the order given by the mesh ordering for direction  $\boldsymbol{\Omega}_d$ .

For general meshes, in particular HO meshes, a mesh element ordering for which the matrix  $F^{(d)}$  is block lower triangular may not exist. Instead, we find a mesh element ordering for which the block upper-triangular matrix,  $F_{>}^{(d)}$ , is as small as possible, where we have decomposed  $F^{(d)}$

in an alternative manner,

$$F^{(d)} = F_{\leq}^{(d)} + F_{>}^{(d)}. \quad (20)$$

Once such a mesh ordering is found, we perform a lagged transport sweep to update  $\psi_{(\ell+1)}^{(d)}$ ,

$$\left[ G^{(d)} + F_{\leq}^{(d)} + M_t \right] \psi_{(\ell+1)}^{(d)} = \mathbf{q}^{(d)} + \frac{1}{4\pi} M_s \varphi_{(\ell)} - F_{>}^{(d)} \psi_{(\ell)}^{(d)}. \quad (21)$$

The iteration scheme described in (21) is equivalent to solving (18) using a block Gauss-Seidel solver on a specific ordering of elements.

We now pose the problem of choosing a good element ordering in a graph-theoretical sense. In particular, for each quadrature direction  $\Omega_d$ , we construct a directed graph whose vertices  $V_e$  correspond to mesh elements  $\kappa_e$ . There exists a weighted oriented edge between mesh element vertices  $(V_e, V_{e'})$  in the graph if  $F_{e,e'}^{(d)}$  is nonzero. The choice of edge weight,  $z_{e,e'}$ , connecting  $(V_e, V_{e'})$  is critical in determining the convergence behavior of (21). In this work, we consider three choices for  $z_{e,e'}$ :

1. Unity,  $z_{e,e'} = 1$ ;
2. Face,  $z_{e,e'} = \|F_{e,e'}\|$ ; and
3. SigInvFace,

$$z_{e,e'} = \left\| (M_{t,e})^{-1} F_{e,e'} \right\|, \quad (22)$$

where  $\|A\| = \max_{i,j} |a_{ij}|$  denotes the maximum element norm of a matrix. Equation (22) accounts for the importance of effective streaming area while also taking into account that radiation is less likely to stream across optically thick mesh elements.

In order to compute a good element ordering, we solve the corresponding maximum acyclic subgraph problem, also known as the feedback arc set (FAS) problem [9]. In particular, each element ordering corresponds to some number of forward edges  $(V_e, V_{e'})$ ,  $e' > e$ , and some number of backward edges  $(V_e, V_{e'})$ ,  $e' \leq e$ . We find an element ordering that minimizes the weight associated with the forward edges,

$$\sum_e \sum_{e' < e} z_{e,e'},$$

because the collection of forward edges corresponds to the upper block-triangular part of the

matrix. This collection defines the outgoing face matrices  $F_{e,e'}$  that are applied to lagged data within the transport sweep (21). Although this problem is known to be NP-hard (see, for example, [9]), efficient heuristic methods can be used to compute an approximate solution.

To determine a mesh-element sweep ordering, we first compute all strongly connected components (SCCs) of the graph [25]. Then, we use the fact that a globally minimum FAS can be determined by independently computing on each SCC a minimal FAS. Since most SCCs involve only a few elements, this often allows the computation of a minimal FAS without approximation using integer programming. If the number of vertices in individual SCCs is larger than a constant, say 10, we determine an (approximate) minimum FAS using the heuristic algorithm of [9].

## IV. RESULTS

In this section we present results in the context of  $S_N$  transport on high-order curved meshes. We focus on the properties of cycle breaking and iterative convergence with respect to the mesh curvature and sizes of cycles. Discussion about an alternative approach to handle curved meshes, namely, transition to a low-order linear mesh, is also included.

Convergence properties of the method for the cases of scattering-dominated regimes is beyond the scope of this article. This subject is addressed in [?] where we present a new diffusion synthetic acceleration (DSA) preconditioner for DG discretizations on high-order meshes.

Our implementation of the algorithms presented in the previous sections utilizes the MFEM finite element library [1].

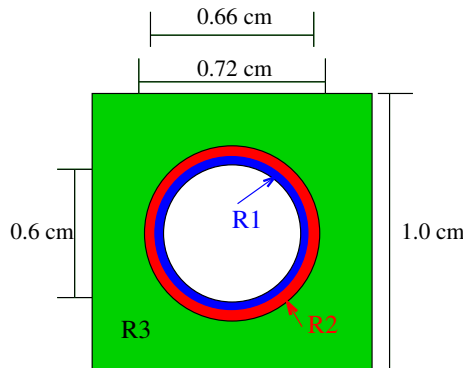
### IV.A. Nested Annuli Test Problem

Our first example is a three region test problem consisting of two nested annuli surrounded by a square domain, similar to the geometry of a pressurized water reactor pincell. It is important to note that the region interior to the annulus is not included in our problem domain. The dimensions of the problem are shown in Fig. 1 and material properties are given in Table I. We solve this

TABLE I  
Annular test problem material properties.

Region	R1	R2	R3
$\Sigma_s$ $cm^{-1}$	1.0	1.0	1.0
$\Sigma_t$ $cm^{-1}$	2.0	2.2	2.4

Fig. 1. Annular test problem geometry.



problem on a series of meshes of cubic elements using cubic DG representations of the angular flux,

- HO coarse- 540 cubic mesh elements (Fig. 2(a)),
- HO refined- 2160 cubic mesh elements (Fig. 2(b)),

and low-order, spatially refined meshes,

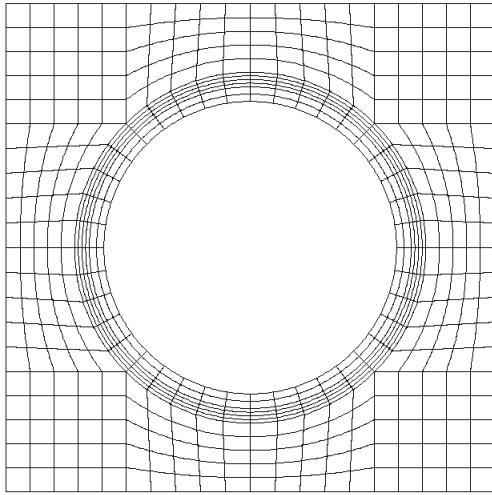
- Straightened coarse- 4860 linear mesh elements (Fig. 2(c)), and
- Straightened refined- 19440 linear elements (Fig. 2(d)).

The low-order, spatially refined, or “straightened,” meshes are generated in MFEM [1] by projecting a HO mesh onto a linear mesh. This is achieved by dividing each element  $N_{ref}$  times in every direction. The vertices of these sub-divided elements are then taken to be the nodes of the linear mesh. This process is demonstrated qualitatively in Fig. 3.

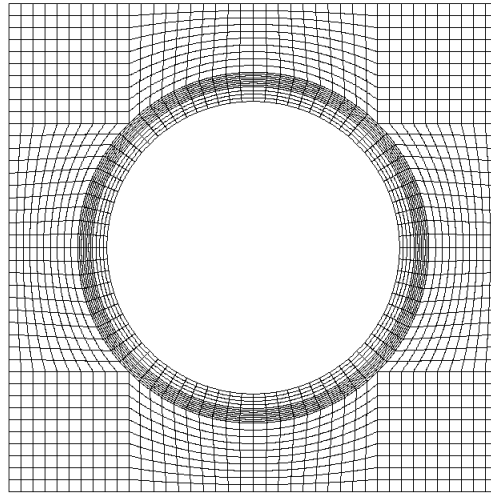
Straightening a HO mesh and solving on the LO mesh using LO finite elements is an alternative to solving the linear transport equations directly on the HO mesh using HO finite elements. Such an approach is appealing in that it,

1. permits the use of existing, highly-optimized transport solvers designed for meshes of linear elements,
2. likely results in fewer and smaller mesh cycles, if our graph based sweep is too inefficient, and

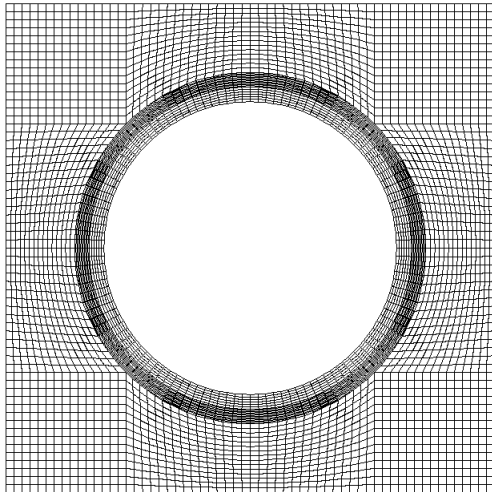
Fig. 2. Meshes for annular test problem.



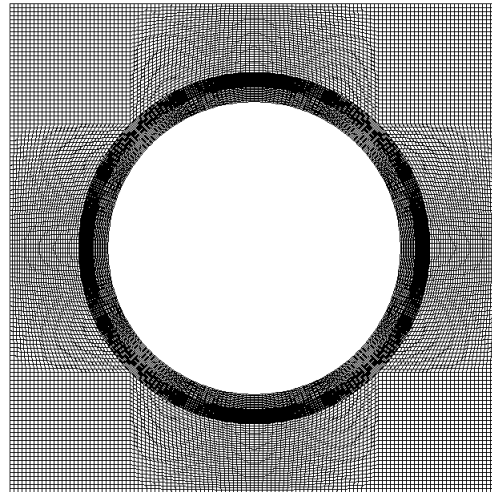
(a) Coarse HO mesh.



(b) Refined HO mesh.



(c) Coarse straightened mesh.

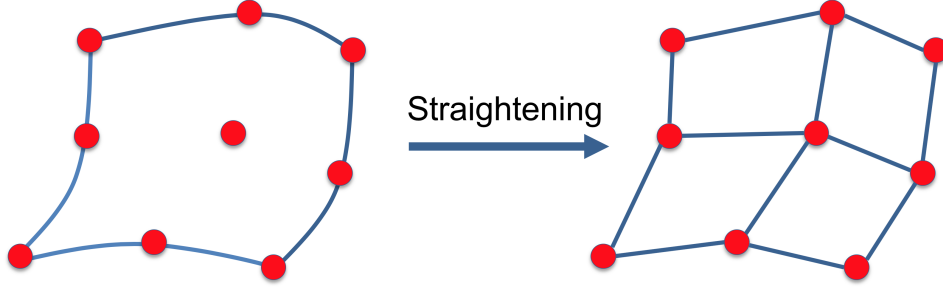


(d) Refined straightened mesh.

3. probably generates fewer negative angular flux solutions, because the mesh would be more spatially refined, and low-order finite elements typically generate fewer negativities in spatially under-resolved regions compared with HO finite elements.

The above benefits hold true under several *conditions* that are listed below. We stress that, up to our knowledge, the current literature doesn't contain any methods for transition between HO and LO meshes that could provide all of the listed conditions:

Fig. 3. Qualitative description of the straightening procedure.



1. a spatially refined, valid LO mesh can be easily generated from any given HO mesh,
2. mapping materials and interfaces from the HO mesh to the LO mesh does not degrade solution accuracy,
3. the relative speed of existing, transport solvers operating on a refined LO mesh can compensate for the increase in number of unknowns, and
4. the computational time required for mapping of fields from the HO mesh to the LO mesh and back is trivial.

Using the method of manufactured solutions [15, 24], we first demonstrate that HO solutions on HO meshes are more accurate than LO solutions on LO refined meshes on problems with curved boundaries. We impose a solution of the form

$$\psi_d(x, y) = \left[ \frac{1}{2}(1 + x^2 + y^2) + \cos\left(3x + \frac{3y}{2}\right) \right] [\mathbf{\Omega}_{d,\mu}^2 + \mathbf{\Omega}_{d,\eta}], \quad (23)$$

where  $\mathbf{\Omega}_{d,\mu}$  and  $\mathbf{\Omega}_{d,\eta}$  are the direction cosines with respect to the  $x$ - and  $y$ -axes, respectively. Using  $S_4$  level-symmetric angular quadrature, we tabulate the  $L_2$  error of the scalar flux solution in Table II. As shown in Table II, HO transport solutions on HO meshes are orders of magnitude more accurate than LO refined solutions, despite the HO methods using significantly fewer unknowns.

The number of mesh cycles for each HO mesh is summarized in Table III. Note that, given the symmetry of this problem and the quadrature set used, we only provide the mesh-cycle information for two angle types,

1. the “diagonal” ordinates:  $\mathbf{\Omega}_{d,\mu} = \mathbf{\Omega}_{d,\eta}$ , and

TABLE II  
Comparison of  $L_2$  errors for MMS on annular test problem.

	Error	Number of $\tilde{\varphi}(\mathbf{x})$ Unknowns
Straightened Coarse	$2.603 \times 10^{-5}$	19940
Straightened Refined	$4.946 \times 10^{-6}$	77760
HO Coarse	$2.5731 \times 10^{-7}$	8640
HO Refined	$1.491 \times 10^{-8}$	34560

TABLE III  
Mesh Cycles in Nested Annuli Test Problem.

Mesh	Angle	Total Cycles (Simple+ <b>Large</b> )	Elements in Large SCC	Total Edges Removed
HO Coarse	Diagonal	12 + <b>0</b>	-	12
	Off-Diagonal	2 + <b>2</b>	[7,7]	14
HO Fine	Diagonal	24 + <b>0</b>	-	24
	Off-Diagonal	6 + <b>4</b>	[3,3,13,13]	34

2. “off-diagonal” ordinates (every other discrete ordinate direction).

Note that for this particular problem, unity weighting of inter-element dependencies was used, but the choice of graph-edge weighting did not affect the number of edges removed to make an acyclic sweep ordering.

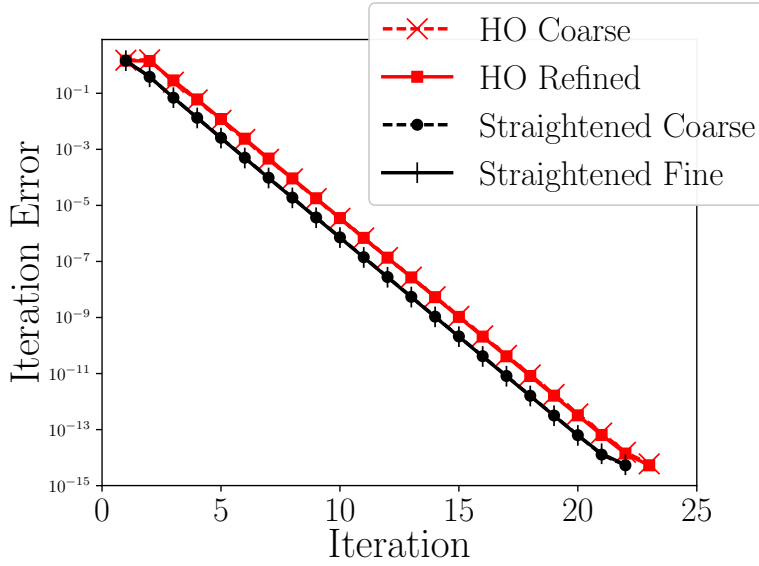
In Fig. 4, we demonstrate that, despite the HO annular meshes having mesh cycles, with the graph-based sweep ordering, the mesh cycles do not significantly degrade iterative convergence, requiring one additional iteration to reach the same convergence criterion. Figure 4 plots the computed iteration error, taken to be the  $L_\infty$  norm of the difference of successive iterates,

$$\log_{10} \left( \max_d \left\| \boldsymbol{\psi}_{j+1}^{(d)} - \boldsymbol{\psi}_{j+1}^{(d)} \right\|_\infty \right),$$

versus the fixed-point iteration index. Source iteration for this problem is terminated when the norm of the difference of successive iterates is near machine precision,  $10^{-14}$ .

The nested annuli test problems shows that HO transport on HO meshes can be more accurate with fewer unknowns than LO transport discretization on spatially refined grids, as shown by Table II. Additionally, the nested annuli test problem shows that HO meshes introduce mesh cycles that LO meshes do not possess (see Table III). However, as shown in Fig. 4, this mesh cycling does not significantly degrade iterative convergence relative to cycle-free, straightened meshes of the same

Fig. 4. Iterative convergence for the nested annuli test problem.

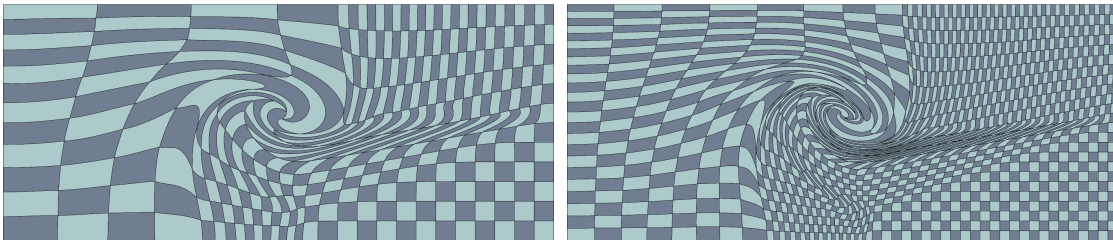


problem.

#### IV.B. Triple-point Problem

Our next example uses an underlying mesh generated from a purely Lagrangian simulation of the “triple point” problem [12] using cubic discretizations of the kinematic variables, creating third-order meshes. The low resolution and high resolution variants of this mesh are shown in Fig. 5(a) and Fig. 5(b), respectively. The scattering and total cross sections are constant,  $\Sigma_s = 1 [cm^{-1}]$  and  $\Sigma_t = 2 [cm^{-1}]$ , the problem is driven by an isotropic source  $q_d(\mathbf{x}) = 1 + \sin^2(2x + y)$  and a constant inflow boundary condition of unity for all discrete ordinate directions. An  $S_2$  level symmetric angular quadrature set is used to discretize the problem in angle.

Fig. 5. HO triple-point meshes.



(a) Cubic mesh with 336 elements.

(b) Cubic mesh with 1344 elements.

As seen in Fig. 5, this problem effectively represents a worst case scenario for mesh cycling in a two-dimensional problem. We use this problem to demonstrate:

1. it is possible to sweep on HO meshes with very large strongly connected components,
2. different graph weightings can result in different source iteration convergence rates, and
3. mesh straightening is in general impractical.

First, we give the number of mesh cycles present in the HO meshes we consider in Table IV. In Table IV and Table V,  $a = \frac{\sqrt{3}}{3}$ . While the number of elements in each SCC is independent of the edge weighting used, the number of edges removed from the graph is not. Table V shows the number of edges removed in solving the FAS sweep ordering problem for each edge-weighting method considered.

TABLE IV  
SCC information for the HO triple-point problem.

Mesh	Angle	Total Cycles (Simple+ <b>Large</b> )	Elements in Large SCC
336 Elements	$\langle a, a \rangle$	0 + <b>1</b>	[97]
	$\langle -a, a \rangle$	1 + <b>1</b>	[46]
	$\langle a, -a \rangle$	1 + <b>1</b>	[46]
	$\langle -a, -a \rangle$	0 + <b>1</b>	[97]
1344 Elements	$\langle a, a \rangle$	0 + <b>1</b>	[475]
	$\langle -a, a \rangle$	1 + <b>2</b>	[3,184]
	$\langle -a, a \rangle$	1 + <b>2</b>	[3,184]
	$\langle -a, -a \rangle$	0 + <b>1</b>	[475]

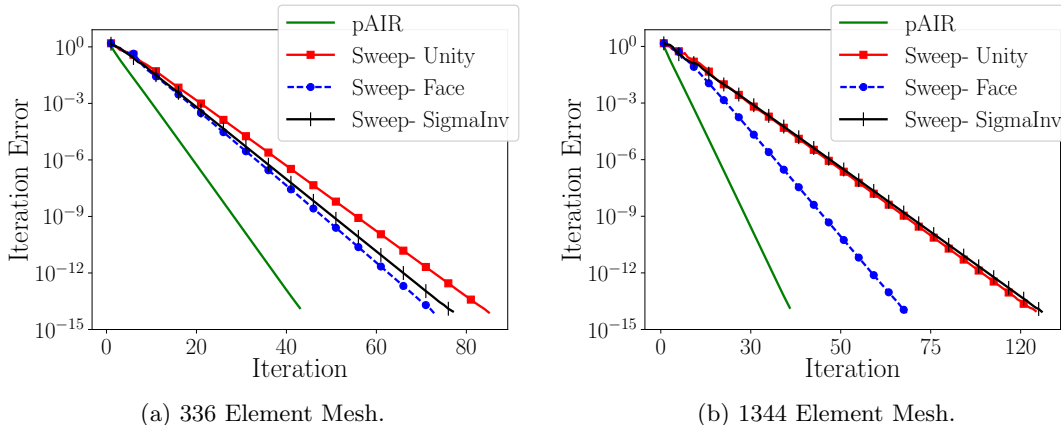
TABLE V  
Edges removed to define a sweep ordering for the HO triple-point problem.

Mesh	Angle	Edge Weighting		
		Unity	Face	SigmaInvFace
336 Elements	$\langle a, a \rangle$	60	63	72
	$\langle -a, a \rangle$	25	30	39
	$\langle a, -a \rangle$	26	31	36
	$\langle -a, -a \rangle$	66	64	82
1344 Elements	$\langle a, a \rangle$	144	170	292
	$\langle -a, a \rangle$	68	91	143
	$\langle a, -a \rangle$	81	100	112
	$\langle -a, -a \rangle$	202	209	285

To assess how the upwind dependency lagging required to sweep mesh element by element affects overall scattering source iteration, we compare against an “ideal” fixed-point, solving Eq.

(18) directly without the Gauss-Seidel iteration introduced by sweeping on HO grids [see Eq. (21)]. We solve Eq. (18) using a recently developed algebraic multigrid method for non-symmetric matrices, referred to as *pAIR* [17, 16]. Iterative convergence for both meshes is plotted in Fig. 6. As shown in Fig. 6, sweeping element-by-element does incur an iteration effectiveness penalty, but

Fig. 6. Iterative convergence for triple-point problem.



still converges at a reasonable rate, even for problems with large SCCs.

Finally, we use the HO triple-point meshes to demonstrate that in general, it is at best impractical to straighten HO meshes. For this study, we simply seek the minimum refinement level necessary to yield a low-order, spatially refined mesh that satisfies  $|J(\xi)| > 0$  at every node.

Straightening of the purely Lagrangian triple-point meshes to yield positive  $|J(\xi)|$  everywhere in the low-order mesh is not always possible, e.g., as in the case with the 1344 element mesh. Furthermore, straightening is likely to be impractical as shown by the 336 element mesh needing 24 levels of refinement to yield strictly positive  $|J(\xi)|$ . In particular, refining the HO mesh by a factor of 24, to create a low-order mesh for low-order transport, would increase the number of transport unknowns by a factor of 144 for this problem. Attempts were made to use up to 180 refinements to straighten the 1344 element HO mesh, however we could not verify that even at that level of refinement the straightened mesh had  $|J(\xi)| > 0$  at every node.

#### IV.C. 3D Rayleigh-Taylor problem

In our final example we consider a three-dimensional third-order mesh generated via a purely Lagrangian simulation of a 3D variation of the classic Rayleigh-Taylor instability problem [8]. The

mesh contains 256 zones and is shown in Figure 7. This problem demonstrates that sweeping is still possible on highly-distorted 3D meshes.

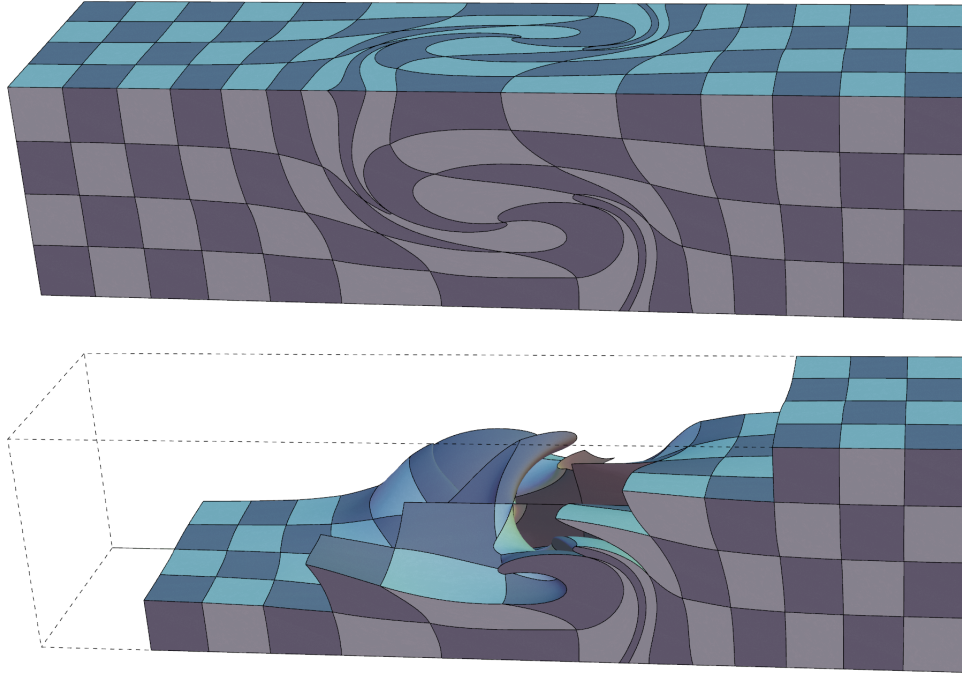


Fig. 7. Cubic 3D mesh (top) resulting from a Lagrangian simulation of the Rayleigh-Taylor problem. A subset of the mesh elements is shown on bottom.

Like the triple-point problem, the 3D Rayleigh-Taylor problem also illustrates a case when straightening the HO mesh is not a feasible alternative, due to the high curvature of the original mesh. In particular, obtaining a valid, LO refined version of a coarser variant of this problem, 32 third order zones, requires refining each HO mesh element by a factor of 15, resulting in a linear mesh containing 108000 elements with 864000 transport spatial degrees of freedom versus 32 HO elements and 2048 transport spatial degrees of freedom.

The scattering and total opacities are constant throughout the domain,  $\sigma_s = 1$  and  $\sigma_t = 2$ , and we set a constant inflow boundary condition of unity for all discrete ordinate directions. An  $S_2$  level symmetric angular quadrature set is used to discretize the problem in angle. The problem is driven by the following volumetric source:

$$q_d(\mathbf{x}) = 1 + \sin^2(4x + 2yz + 2y) .$$

Each of the eight discrete ordinate direction develops one SCC containing 79 or 83 elements, out of 256 elements in the full mesh. The number of removed graph edges for each of the three weighting strategies are listed in Table VI. The Unity, Face, and SigmaInvFace strategies converge in 79, 78, and 83 iterations, respectively, with very similar convergence histories. The final solution and convergence history with the SigmInvFace strategy are shown in Figure 8.

TABLE VI  
Edges removed to define a sweep ordering for the 3D Rayleigh-Taylor problem.

Angle	Elements in Large SCC	Edge Weighting		
		Unity	Face	SigmaInvFace
$\langle a, a, a \rangle$	83	106	104	123
$\langle -a, a, a \rangle$	79	90	93	103
$\langle a, -a, a \rangle$	83	102	103	120
$\langle -a, -a, a \rangle$	79	94	89	112
$\langle a, a, -a \rangle$	79	95	93	108
$\langle -a, a, -a \rangle$	83	111	104	123
$\langle a, -a, -a \rangle$	79	98	89	113
$\langle -a, -a, -a \rangle$	83	102	103	120

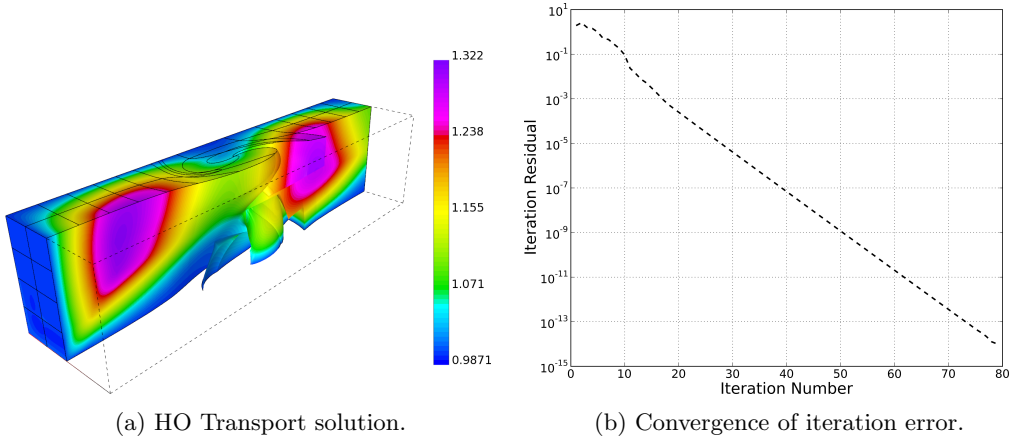


Fig. 8. Final solution and convergence of iterative error for sweeping on the Rayleigh-Taylor mesh.

## V. CONCLUSION AND FUTURE WORK

Solving the linear transport equations directly on HO grids is a requirement for next-generation radiation hydrodynamics simulations. We have demonstrated that, despite a potentially large number of mesh cycles, the linear transport equations can be solved directly on HO meshes by introducing an appropriate mesh ordering on which to do a transport sweep. The ordering is

determined by approximately solving the feedback arc set (FAS) problem, for some measure of distance between mesh elements. Three such distances, or “weightings,” were explored, the unity weighting, face weighting, and sigma-inverse face weighting (see Section IV.C). In all tested cases, the face weighting was the most effective, in one case offering a near  $2\times$  improvement in total iteration count over the unity weighting and sigma-inverse face weighting (see Figure 6). Solving directly on HO meshes eliminates the need to transition to a straightened linear mesh, improves solution accuracy, and requires fewer degrees of freedom.

A future area of research will be the preservation of angular flux positivity when using high-order discontinuous Galerkin spatial discretizations of the linear transport equations in spatially under resolved regions, as well as a more rigorous understanding of the optimal weighting for the FAS problem. We will also explore the challenges HO meshes may pose to diffusion-based synthetic acceleration techniques required for scattering-dominated regimes. Such capabilities are required by multi-material problems involving optically thick and thin transitions. The long-term goal is to derive a time-dependent, nonlinear TRT solver utilizing the iterative techniques described within this work.

## ACKNOWLEDGEMENTS

The work of T. S. Haut, P. G. Maginot, V. Z. Tomov, T. A. Brunner, and T. S. Bailey was performed under the auspices of the U.S. Department of Energy by Lawrence Livermore National Laboratory under contract DE-AC52-07NA27344 and supported by the LLNL-LDRD Program under Project No. 18-ERD-002.

The work of B. S. Southworth was performed under the auspices of the U.S. Department of Energy by Lawrence Livermore National Laboratory under contract DE-AC52-07NA27344 and supported by sub-contracts B614452, and B627942 of Lawrence Livermore National Security, LLC. Additional funding for B. S. Southworth was provided under grant number (NNSA) DE-NA0002376.

This work has been reviewed for unlimited public release as LLNL-JRNL-759880-DRAFT.

## DISCLAIMER

This document was prepared as an account of work sponsored by an agency of the United States government. Neither the United States government nor Lawrence Livermore National Security, LLC, nor any of their employees makes any warranty, expressed or implied, or assumes any legal liability or responsibility for the accuracy, completeness, or usefulness of any information, apparatus, product, or process disclosed, or represents that its use would not infringe privately owned rights. Reference herein to any specific commercial product, process, or service by trade name, trademark, manufacturer, or otherwise does not necessarily constitute or imply its endorsement, recommendation, or favoring by the United States government or Lawrence Livermore National Security, LLC. The views and opinions of authors expressed herein do not necessarily state or reflect those of the United States government or Lawrence Livermore National Security, LLC, and shall not be used for advertising or product endorsement purposes.

## REFERENCES

- [1] MFEM: Modular finite element methods library. *<http://mfem.org>*.
- [2] M. L. Adams and P. F. Nowak. Asymptotic analysis of a computational method for time- and frequency- dependent radiative transfer. *Journal of Computational Physics*, 46:366–403, 1998.
- [3] Robert W. Anderson, Veselin A. Dobrev, Tzanio V. Kolev, Robert N. Rieben, and Vladimir Z. Tomov. High-order multi-material ALE hydrodynamics. *SIAM J. Sci. Comp.*, 40(1):B32–B58, 2018.
- [4] G. Bell and S. Glasstone. *Nuclear Reactor Theory*. Van Nostrand Rienhold, Inc., New York, NY, 1970.
- [5] Walter Boscheri and Michael Dumbser. High order accurate direct arbitrary-Lagrangian-Eulerian ADER-WENO finite volume schemes on moving curvilinear unstructured meshes. *Comput. Fluids*, 136:48–66, 2016.
- [6] B. R. de Supinski. Sierral the LLNL IBM CORAL system. In *12th International Conference on Parallel Processing and Applied Mathematics*, September 2017.

- [7] V. Dobrev, T. Ellis, Tz. Kolev, and R. Rieben. High-order curvilinear finite elements for axisymmetric Lagrangian hydrodynamics. *Comput. Fluids*, pages 58–69, 2013.
- [8] V. Dobrev, Tz. Kolev, and R. Rieben. High-order curvilinear finite element methods for Lagrangian hydrodynamics. *SIAM J. Sci. Comp.*, 34(5):606–641, 2012.
- [9] Peter Eades, Xuemin Lin, and W. F. Smyth. A fast and effective heuristic for the feedback arc set problem. *Information Processing Letters*, 47(6):319–323, 1993.
- [10] J. A. Rathkopf et al. KULL: LLNL’s ASCI inertial confinement fusion simulation code. In *PHYSOR 2000 American Nuclear Society Topical Meeting on Advances in Reactor Physics and Mathematics and Computation into the Next Millenium*, May 7-11 2000.
- [11] Jean-Luc Guermond, Bojan Popov, and Vladimir Tomov. Entropy-viscosity method for the single material Euler equations in Lagrangian frame. *Comput. Methods Appl. Mech. Eng.*, 300:402–426, 2016.
- [12] M. Kucharik, R. V. Garimella, S. P. Schofield, and M. J. Shashkov. A comparative study of interface reconstruction methods for multi-material ALE simulations. *Journal of Computational Physics*, 229:2432–2452, 2010.
- [13] Lawrence Livermore National Lab. hypre version 2.14.
- [14] E. E. Lewis and W. F. Miller. *Computational Methods of Neutron Transport*. American Nuclear Society, La Grange Park, IL, 1993.
- [15] C. Lingus. Analytical tests cases for neutrons and radiation transport codes. In *Second Conference on Transport Theory*, pages 655–659, Los Alamos, New Mexico, January 1971. United States Atomic Energy Commision- Division of Technical Information.
- [16] T A Manteuffel, S Münzenmaier, J W Ruge, and B S Southworth. Nonsymmetric Reduction-based Algebraic Multigrid. *SIAM Journal on Scientific Computing*, (submitted), June 2018.
- [17] T A Manteuffel, J W Ruge, and B S Southworth. Nonsymmetric Algebraic Multigrid Based on Local Approximate Ideal Restriction ( $\ell$ AIR). *SIAM Journal on Scientific Computing*, (accepted), Sep. 2018.

- [18] William III McLendon, Bruce Hendrickson, Steve Plimpton, and Lawrence Rauchwerger. Finding Strongly Connected Components in Parallel Transport Sweeps. In *SPAA 2001*, pages 328–329, 2001.
- [19] J. E. Morel, T. A. Wareing, and K. Smith. A linear-discontinuous spatial differencing scheme for  $S_N$  radiative transfer calculations. *Journal of Computational Physics*, 128:445–462, 1996.
- [20] Shawn Pautz. An Algorithm for Parallel Sn sweeps on Unstructured Meshes. *Nuclear Science and Engineering*, 140:111–136, 2002.
- [21] Shawn D Pautz and Teresa S Bailey. Parallel Deterministic Transport Sweeps of Structured and Unstructured Meshes with Overloaded Mesh Decompositions. *Nuclear Science and Engineering*, 185(1):70–77, 2017.
- [22] Steven J Plimpton, Bruce Hendrickson, Shawn P Burns, William McLendon, and Lawrence Rauchwerger. Parallel Sn sweeps on unstructured grids: Algorithms for prioritization, grid partitioning, and cycle detection. *Nuclear Science and Engineering*, 150(3):267–283, 2005.
- [23] W. H. Press, S. A. Teukolsky, W. T. Vetterling, and B. P. Flannery. *Numerical Recipes: The Art of Scientific Programming*. Cambridge University Press, New York, 3rd edition, 2007.
- [24] K. Salari and P. Knupp. Code verification by the method of manufactured solutions. Technical Report SAND2000-1444, Sandia National Labs, 2000.
- [25] R. Tarjan. Depth-first search and linear graph algorithms. *SIAM Journal on Computing*, 1(2):146–160, 1972.
- [26] T. A. Wareing, J. M. McGhee, J. E. Morel, and S. D. Pautz. Discontinuous finite element  $s_n$  methods on three-dimensional unstructured grids. *Nuclear Science and Engineering*, 138:256–268, 2001.
- [27] D. Woods. High-order finite elements  $s_n$  transport in  $x - y$  geometry on meshes with curved surfaces in the thick diffusion limit. Master’s thesis, Oregon State University, 2016.
- [28] D. Woods, T. A. Brunner, and T. S. Palmer. High-order finite elements  $s_n$  transport in  $x - y$  geometry on meshes with curved surfaces. *Transactions of the American Nuclear Society*, 114:377–380, 2016.

- [29] D. Woods and T. Palmer. Diffusion Synthetic Acceleration for High Order SN Transport on Meshes with Curved Surfaces. In *Trans. of the Am. Nucl. Soc. (June 2017 ANS meeting)*, 2017.